Powder Technology 360 (2020) 1177–1191

Contents lists available at ScienceDirect

Powder Technology

journal homepage: www.elsevier.com/locate/powtec

The impact of self-sustained oscillations on particle residence time in a commercial scale spray dryer

Hasan Jubaer [a], Sepideh Afshar [a], Guénolé Le Maout [b], Serge Mejean [b], Cordelia Selomulya [a,c], Jie Xiao [d], Xiao Dong Chen [d], Romain Jeantet [b], Meng Wai Woo [a,e,*]

[a] Department of Chemical Engineering, Faculty of Engineering, Monash University, Victoria, Australia
[b] UMR 1253 STLO, Agrocampus Ouest, INRA, F-35042 Rennes, France
[c] School of Chemical Engineering, The University of New South Wales (UNSW), Sydney, NSW 2052, Australia
[d] Suzhou Key Laboratory of Green Chemical Engineering, School of Chemical and Environmental Engineering, College of Chemistry, Chemical Engineering and Materials Science, Soochow University, Suzhou, Jiangsu, China
[e] Department of Chemical and Materials Engineering, The University of Auckland, New Zealand

ARTICLE INFO

Article history:
Received 20 July 2019
Received in revised form 2 November 2019
Accepted 8 November 2019
Available online 9 November 2019

Keywords:
CFD
Unsteady
Residence time
Spray drying
Cylinder-on-cone
Flow field

ABSTRACT

Spray drying is an established technique, which widely employs cylinder-on-cone type chambers. The air flow patterns inside such chambers are usually governed by transient fluctuations, which impact particle movement and drying history. To understand this impact, CFD using Lagrangian particle tracking through Eulerian flow-field was employed. The simulations revealed transient flow structures due to central jet deflections followed by rotating upwards sweep and formation of vortices. The self-sustained-fluctuations were intensified by high velocity of the main hot air inlet, while lower temperature thereof led to smoother fluctuations. Detailed numerical analyses on particles sampled at the outlet revealed that the distinct transient flow-field actually reduced the particle residence time compared to the residence time estimated via a simplified method ignoring flow-field fluctuations, while generating a wider distribution. No simple correlation was ascertained between the particle size and the residence time distributions, which indicates all sizes considered in the work are affected similarly by the air flow. These findings will benefit the designing of spray dryers.

1. Introduction

The cylinder-on-cone type of spray dryer is widely used in industry particularly in the production of dairy powders. In modern spray drying operation of manufacturing dairy powders involving two- or three-stage drying, a static fluidized bed is often built into the bottom section of the cone, which constitutes the second stage of drying [1–3]. For such a spray drying configuration, the air flow within the chamber primarily consists of a central annular hot air jet entering the dryer at the middle of the chamber ceiling. The jet then traverses the height of the chamber in a downward direction, while the distance of traversing is influenced by the inlet air flow for the static fluidized bed at the bottom. The central jet then gets mixed with the fluidized bed inlet and start flowing upwards the conical region. The typical air outlet is normally located either at the top or towards the side of the tower.

It is well known that such a confined jet flow exhibits self-sustained oscillation behavior [4–6]. To be more specific, the oscillation manifests its behavior as fluctuating flaps of the central jet deviating from the axis of the chamber. This behavior was experimentally observed in large commercial spray dryers [7] as well as in small scale spray dryers [8]. Kieviet, Van Raaij, De Moor and Kerkhof [9] reported some fluctuations in the slow recirculation regions away from the axis and in the proximity of the wall. The fluctuations mean that even when the spray dryer is operated at steady state conditions, the air flow behavior within the chamber remains markedly dynamic. In particular, the upwards air flow pattern and the recirculation region within the chamber changes continuously due to the fluctuation behavior.

Simulation works have shown that these self-sustained fluctuations can primarily be attributed to pressure imbalances at regions adjacent to the central jet [10,11]. Numerical explorations have shown that larger chamber diameter at relatively lower inlet jet velocity will potentially ease the pressure imbalance, eventually eliminating the self-sustained fluctuation [5]. In a series of reports [6,10,12], it was suggested that the oscillation behavior is directly related to the expansion ratio between the diameter of the inlet jet and the chamber diameter. At any rate, such self-sustained fluctuation behavior is well established and its impact on the numerical approach to modelling spray drying

Abbreviations: CDC, Characteristic Drying Curve; CFD, Computational Fluid Dynamics; GAB, Guggenheim-Anderson-de Boer (model); MDSD, Mono-Disperse Spray Drying; PSD, Particle Size Distribution; REA, Reaction Engineering Approach; RR, Rosin-Rammler distribution; SDD, Single Droplet Drying; SST, Shear Stress Transport model; UDF, User Defined Function.

* Corresponding author.
E-mail address: wai.woo@auckland.ac.nz (M.W. Woo).

https://doi.org/10.1016/j.powtec.2019.11.023
0032-5910/

processes using computational fluid dynamics (CFD) has been justifiably discussed in the literature by many researchers [5,6,10,13].

One of the major phenomena directly affected by these air flow fluctuations is particle movements within the chamber, which directly determines the drying history of the particles and consequently the final powder properties such as color, component denaturation, stickiness. The effect of the fluctuation behavior on particle movement within the chamber has not been explicitly investigated, albeit some reports have considered air flow fluctuations in studying the wall deposition. It was claimed that such self-sustained fluctuations of the central jet 'push' particles closer to the wall leading to a more significant deposition [14,15]. Jin and Chen [16] investigated the residence time of particles among other parameters by means of CFD technique in a large-scale industrial dryer and reported that the medium sized particles (225–270 μm) would form particle clusters, which were also found to stay close to the wall and exhibited largest residence time, although due to using the 2D axisymmetric model the self-sustained fluctuation behavior of the air-flow pattern could not be accurately captured in the study. At any rate, to the best of the authors' knowledge, no report has to date focused on how the self-sustained fluctuation behavior, in particular the continuously changing recirculation and upwards flow regions in the chamber, affect particle movements within the spray drying chamber. Understanding this phenomenon is very important, as the movement of a particles governs its residence time within the chamber. This subsequently determines its drying history and ultimately final powder properties.

This work aimed to fill this gap in knowledge by means of numerical analysis of a commercial pilot scale spray dryer having a cylinder-on-cone geometry fitted with a bottom static fluidized bed. It must be noted that Jeantet, Ducept, Dolivet, Méjean and Schuck [17] experimentally studied the residence time distribution of skim milk particles in the same dryer by varying the fine returns and fluidized bed thickness. They found that the increase in the latter resulted in an increase in residence time, while the change in the first had no significant impact. In contrast, this study relies mainly on the simulation predictions to understand the air flow patterns governed by self-sustained fluctuations and the effect thereof on the particle paths as well as residence times. The detailed numerical analysis was undertaken by employing the computational fluid dynamics technique on several case studies with different operating conditions. Experimental data from the trials with whole milk spray drying at corresponding operating conditions provided basis for validation of the computational models. Crucial insights obtained from analyzing the air flow pattern inside the chamber as well as the particle residence time under different fluctuating behavior would significantly contribute in advancing the knowledge pertinent to the design of spray dryers. Furthermore, a simplified method of estimating the residence time of particles was devised in this work. Although the approximation method was adjusted mainly based on CFD results, it is still based on realistic prediction capturing the key physical phenomena in the drying chamber. We opine that this level of accuracy is sufficient to qualify as a particle residence time approximation tool for rough engineering designing purposes. At any rate, it is already an advancement to the current technique employed by the industry. Our literature review revealed no result supported approximation method, let alone an in-depth rigorous method to estimate the residence time. To the best of authors' knowledge, when designing and scaling up of industrial spray-dryers are performed, a crude estimation (presumably tower height divided by velocity) is typically used with experience based contingency factors. As compared to this approach, the newly developed method provides a more realistic approximation, and hence is expected to add a significant contribution to designing large scale spray dryers.

2. Material and methods

2.1. Spray dryer configuration and trials

The Bionov commercial pilot scale spray dryer in INRA (Rennes, France) was used for this study. The system was already employed in a previous study and described elsewhere [17], yet the most relevant details are mentioned here for readers' convenience. Fig. 1 shows the

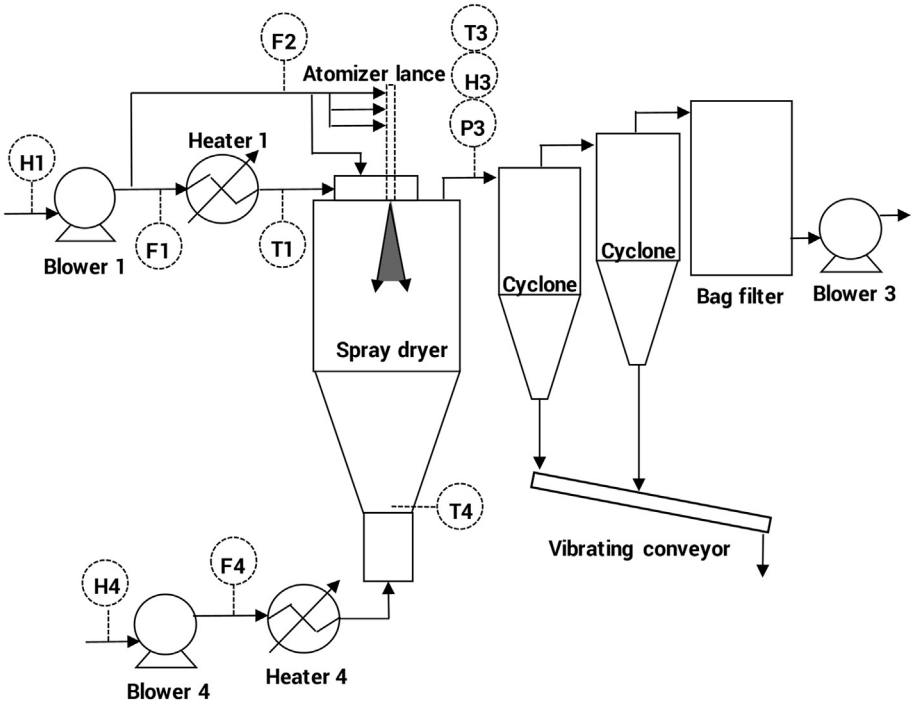

Fig. 1. Key components in the operation of the Bionov used for the trials (atomization line not shown).

key components of the Bionov system utilized for this work. The drying air entering the system is supplied by a common source dehydrated by a main Munters air dehydration system. An important element in plant trials was that the fines were not returned to the atomizer region. There were several reasons for this approach, which are briefly described below (potentially useful for future workers in this area):

Firstly, there existed no measurement of the mass flow rate of fines being recycled. Therefore, if the fines were to be recycled to the top section of the atomizer, sufficient boundary condition information would not be available to simulate fines return. Secondly, returning of the fines to the atomizer region would lead to particle size enlargement due to agglomeration and eventually lead to accumulation on the static fluid bed which is undesired for the purpose of this work (will be explained in the next point). Similarly, the return of fines into the bottom fluidized bed would lead to the undesired formation of the powder bed. Fortuitously, with the operating conditions used in this work, there is negligible accumulation of powder in the bottom static bed with nearly all the powder leaving the chamber via the top outlets to the cyclones. In a trial involving spraying 144 kg of whole milk solids, less than 1 kg was recovered from the bottom fluidized bed. Thirdly, the reason why accumulation on the static fluid bed was undesired was because within the Eulerian-Lagrangian CFD framework, only low particle loading with instantaneous particle-particle contact is modelled. As such only the air flow from the bottom static bed was modelled and not the densely loaded fluidization of powder. This is the current limitation of the Eulerian-Lagrangian based CFD simulation of spray dryers reported in the literature [18].

High pressure single fluid nozzle atomization at 200 bar was used (Spray Dry SK – orifice inset index 72 (0.63 mm), core insert 21, hollow cone spray angle 55°). In all the trials reported here, 40%wt reconstituted whole milk at 45°C was sprayed, which was prepared from commercial whole milk powder (Lactalis, France). Table 1 shows the operating conditions used in the plant trials. The spray rate was maintained approximately the same (±5% variation) throughout the experimental plan. The first 4 trials were aimed at assessing the behavior of the spray dryer at varying inlet temperatures. As the spray rate was maintained the same, the outlet temperature consequently increases with increasing inlet temperature. Although the outlet temperature in run 1 and 2 seemed relatively high compared to typical whole milk powder production, it is noteworthy that the aim of the trials was to generate a wide range of experimental conditions for the validation of the CFD predictive framework. Trial 5, 6 and 7 were primarily aimed at varying the hot air inlet mass flow rate. It was decided for the outlet temperature to be maintained at about 75 or 80 °C, which is a usual range to obtain sufficiently dry powder (i.e. with an water activity a_w around 0.2). For this purpose, lower inlet temperature was used at higher air flow rate and vice versa.

It can be seen that among the trials, there is variation to the cooling air entering the atomizer lance and the plenum chamber of the spray drying chamber. This was because the cooling air and the top hot air inlet share the same blower. An increment in the primary hot air flow rate from 1750 kg/h (Run 7) to 3128 kg/h (Run 6) correspondingly increases the flow rate of the cooling air ranging from 247 kg/h (Run 7) to 317 kg/h (Run 6) and vice versa. In addition, when higher primary hot air temperature such as 250 °C (Run 1) and 215 °C (Run 2) was used, the higher back pressure generated in the hot air line in effect forced more air to the cooling air stream leading to air flow rates of 293 kg/h and 277 kg/h respectively. Similarly, the fluidized bed air flow rate is also affected by the flow rate of the primary hot air. As the operation of blower 4 was maintained constant throughout the trials, when a higher primary air flow rate was used, the higher pressure of the central downwards jet led to lower upwards flow rate from the bottom static bed. For example, in Run 5 for a primary hot air flow rate of 3128 kg/h a static bed air flow rate of 559 kg/h was measured, whereas in Run 7 the flow rates were 1750 kg/h and 721 kg/h respectively.

2.2. Development of the simulation domain and the boundary conditions

In developing the simulation domain significant effort was invested to capture the cooling air configuration of the atomizer lance. This was important as the total cooling air actually contributes to ~10% of the primary drying air flow rate. Fig. 2a shows the configuration of the atomizer lance before installation into the dryer. The four cooling air inlets correspond to the four cooling air streams surrounding the atomizer lance in Fig. 1. The cooling air 1 surrounds the atomizer lance, and the cooling air 3 and 4 are located at the periphery of the setup. The cooling air 2 aims at returning the fines collected from the cyclones to the nozzle outlet in the typical operation of the dryer; however, it was only for cooling purposes in this work as the fines were directly collected at the bottom of the cyclones and mixed with the outgoing powder. A cross-section view of the atomizer lance from the bottom is given in Fig. 2b, illustrating the annular exits of the cooling air. When installed into the air plenum chamber of the dryer, the set of annular cooling air pipes slightly protrude into the chamber (Fig. 2c).

These features of the atomizer lance were incorporated into the simulation domain. This is illustrated in Fig. 3 showing a cross-section of the 3D simulation domain with dimensions of the key features described earlier. All the air inlets were designated as mass flow inlets normal to

Table 1
Conditions for the experimental trials and the dryer outlet and product characteristics.

Parameters	Run 1	Run 2	Run 3	Run 4	Run 5	Run 6	Run 7
Spray rate, L/h	100	103	103	105	101	103	102
Inlet air humidity, g/kg dry air (H1) (H4)	0.9	1.0	0.8	0.9	1.3	1.0	0.8
Primary hot air inlet flow rate, kg/h (F1)	2400	2338	2384	2338	3128	3128	1750
Inner hot air annulus flow rate, kg/h	1795.9	1749.5	1783.9	1749.5	2340.6	2340.6	1309.5
Outer hot air annulus flow rate, kg/h	604.1	588.5	600.1	588.5	787.4	787.4	440.5
Primary inlet air temperature, °C (T1)	250	215	191	186	162	170	223
Cooling air flow rate, kg/h (F2)	293	277	281	260	317	317	247
Cooling air 1 flow rate, kg/h	26.7	25.3	25.6	23.7	28.9	28.9	22.5
Cooling air 2 flow rate, kg/h	142.8	135	137.0	126.7	154.5	154.5	120.4
Cooling air 3 flow rate, kg/h	76.6	72.4	73.4	68.0	82.9	82.9	64.6
Cooling air 4 flow rate, kg/h	46.9	44.3	45.0	41.6	50.7	50.7	39.5
Cooling air temperature, °C	20	20	20	20	20	20	20
Static bed air flow rate, kg/h (F4)	664	664	690	680	559	591	721
Static bed air temp., °C (T4)	72	72	71	71	71	72	70
Outlet pressure, Pa gauge (P3)	−302	−302	−518	−302	−302	−302	−432
Outlet humidity, g/kg dry air (H3)	22.6	22.4	17.5	23.1	19.0	16.4	21.1
Outlet temp., °C (T3)	111	91	80	75	75	81	80
Product moisture content, %wt	1.09	1.65	2.35	2.54	3.32	2.82	2.18

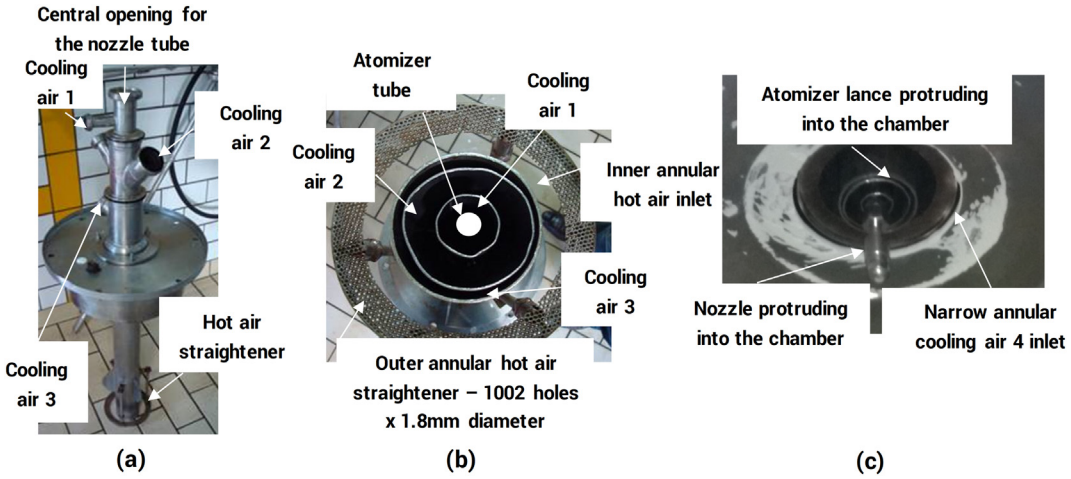

Fig. 2. Illustration of the atomizer lance configuration, (a) before installation into the dryer, (b) view from below showing the annular inlets of the cooling air, (c) after being installed into the chamber showing the protruding parts of the lance.

the boundary while the two outlets at the top of the chamber was specified as pressure outlets, in the simulation domain.

In order to account for the heat loss from the chamber, all walls have been modelled to allow a convective heat transfer with specified heat transfer coefficient of 3 W/m^{2}K and a free stream temperature of 20 °C. The wall material was chosen to be steel with 2 mm thickness. The heat transfer coefficient was specified based on a comprehensive sensitivity analysis on the prediction of the outlet temperature for various cases.

As shown in Fig. 1, the cooling air mass flow rates were only measured at the main pipes before the splitting between the 4 cooling air inlets into the chamber. In the absence of more detailed measurements, the total mass flow rate was divided in proportion of the area of the individual inlet opening. This is a simplifying assumption, in which the

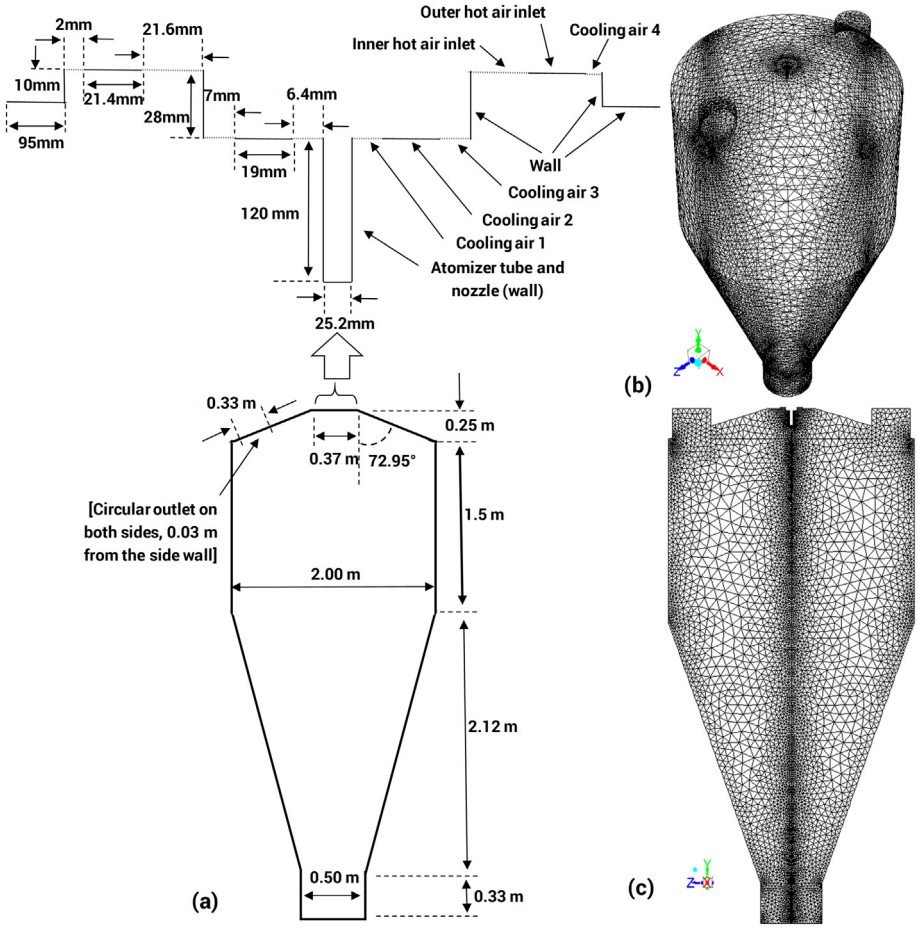

Fig. 3. (a) Simplified schematic of the spray tower with all relevant dimensions (below) and the detailed configuration of the air inlets near the atomizer lance (above). (b) Isometric and (c) cross-sectional (YZ plane) view of the used mesh for the simulation domain.

main factor limiting the air flow rate is based on the size of the opening. In a similar manner, the mass flow rate was split between the inner and outer hot air annulus. The surface area was calculated by the summation of the area of the perforated holes. Turbulent intensity of 5% was assumed for all the inlets and the turbulent length scale at the inlet was assumed to follow the hydraulic diameters of the corresponding inlets.

After performing a comprehensive grid independence test on several grids, a mesh containing 449,575 cells in total was selected based on the criteria governed by reasonable accuracy with acceptable resource requirement. The evidence as well as detailed discussion pertaining to the mesh independence test are provided in supplementary information.

The hollow cone spray was modelled by the built-in cone injection model in Ansys Fluent and was positioned in the axis of the chamber just 1 cm below the geometrical nozzle tube. The cone angle was set to be 55° and no swirl fraction was included. From a simplistic conservation of volumetric flow rate, the initial velocity magnitude of the droplets was estimated to be 89 m/s. The number of streams was 10 and each stream included parcels of 20 different diameters. As a result, during each injection 200 parcels were injected. The 20 different diameters of the initial droplets used in the simulations were evenly spaced between 10 μm and 250 μm.

The initial droplet size distribution was back-calculated from the particle size distribution of the product obtained by using a shrinkage factor of 0.869 (ratio of the final particle size to the initial droplet size). This factor was reported by Lin and Chen [19] for whole milk at initial solid content of 40%. The back-calculated initial droplet size, when fitted to a Rosin-Ramnler distribution, exhibited the following distribution parameters: mean diameter (size constant) – 60.4 μm, maximum diameter – 250 μm, minimum diameter – 10 μm, spread parameter – 1.70. The initial and final particle size distributions clearly showing the incorporation of the shrinkage can be viewed in Fig. 11b.

All material (air, liquid water, water vapor, milk) properties such as viscosity, density, heat capacity were modelled by accounting for the temperature dependence according to the correlations reported elsewhere [20].

2.3. Droplet drying modelling

In order to save computational resources during CFD simulations, lumped parameter models were preferred over distributed parameter approach to capture the kinetics of droplet drying. However, the review of literature with respect to the most commonly used lumped parameter approaches revealed that no previous study has hitherto used either characteristic drying curve (CDC) approach [21,22] or the reaction engineering approach (REA) [23] to model the drying of whole milk with 40% initial concentration. Chen and Lin [24] showed by comparing the experimental data for skim and whole milk at 20% and 30% initial concentration with model predictions obtained from both REA and CDC approaches that the REA provided closer agreement, where the maximum deviations for predictions by CDC and REA from measurements were reported to be 3.8% and 1.6% for skim milk and 1.1% and 3.0% for whole milk respectively. Comparing the performance of both models in CFD simulations also confirmed that the discrepancy was below 3% [25,26].

Despite the relatively better performance of REA, the well-established sensitivity of REA to the initial solid concentration [27] made it unsuitable for use in this study due to the unavailability of data for 40% whole milk. In contrast to REA, the CDC approach accounts for the effect of different initial solid concentration by changing the critical moisture content, which corresponds to the moisture content denoting the transition from constant rate drying period to falling rate drying period. Utilizing this advantage, the experimental data for 20% and 30% whole milk were extracted from published [19,24,28] and unpublished reports [29] to derive the parameters needed for the CDC approach.

In general, for lumped parameter models such as CDC, assuming a uniform temperature distribution inside the particle a simple energy balance is used to define the heat transfer between the continuous and discrete phase:

$$m_p c_p \frac{dT_p}{dt} = hA_p(T_\infty - T_p) - \Delta h_{v,i}\frac{dm_{i,p}}{dt} \tag{1}$$

According to the CDC approach the mass transfer between the particle and the drying air can be characterized by the following expression with A_p, h_m, $\rho_{i,\,surf}$ and $\rho_{i,\,\infty}$ representing the particle surface area, mass transfer coefficient, surface and bulk concentration of the evaporating species respectively:

$$\frac{dm_{i,p}}{dt} = fA_p h_m \left(\rho_{i,surf} - \rho_{i,\infty}\right) \tag{2}$$

The heat and mass transfer coefficients were calculated employing the well-known Ranz-Marshall equations [30,31]:

$$Nu = \frac{hd_p}{k_\infty} = 2.0 + 0.6\ Re^{1/2}\ Pr^{1/3} \tag{3}$$

$$Sh = \frac{h_m d_p}{D_i} = 2.0 + 0.6\ Re^{1/2} Sc^{1/3} \tag{4}$$

It is well known that the shrinkage of the particles during drying would affect the heat and mass transfer area as well as the mass transfer coefficient. These effects of shrinkage including how incorporating shrinkage the droplet drying model can be implemented in CFD simulations of spray dryer are comprehensively discussed in a previous work [32] and hence are not being included in this work for brevity. In the Eq. (2), the factor f accounts for the drying kinetics, particularly the inhibition in drying rate affected by the change in internal mass transfer resistance during the falling rate drying period. Usually the following mathematical description is used for the inhibition factor:

$$f = \begin{cases} 1, X \geq X_{cr} \\ \left(\dfrac{X - X_{eq}}{X_{cr} - X_{eq}}\right)^n, X < X_{cr} \text{ with } n = 1 \end{cases} \tag{5}$$

where the parameter "n" being the material-specific factor, governs the linear, concave or convex shape of the characteristic drying curve and must be determined by experiment. In our study however, while investigating the collected data, it was ascertained that the shape of the curve was strictly non-linear and rather resembled an "s-curve"(see Fig. 4).

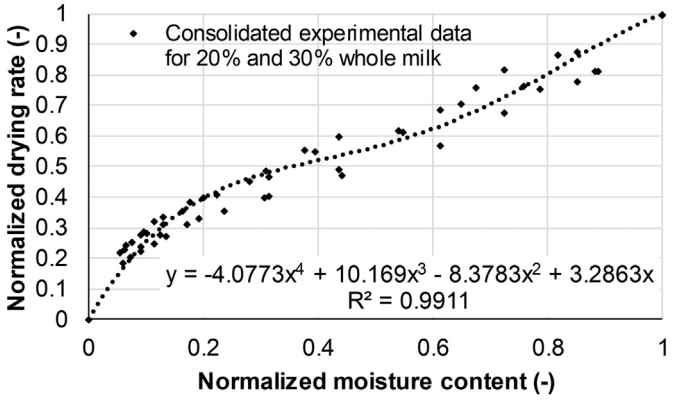

Fig. 4. Determination of the characteristic drying curve for whole milk. Experimental data were extracted from published [19,24,28] and unpublished works [29].

Therefore, a polynomial equation was fitted to better describe the drying curve.

$$f(x) = -4.0773\,x^4 + 10.169\,x^3 - 8.3783\,x^2 + 3.2863\,x \tag{6}$$

with x representing the normalized moisture content $\left(\frac{X - X_{eq}}{X_{cr} - X_{eq}}\right)$, where the critical moisture content X_{cr} was assumed to be the initial moisture content.

The equilibrium moisture content, X_{eq} was determined from the sorption isotherm described by the Guggenheim-Anderson-de Boer (GAB) model:

$$X_{eq} = \frac{Ck_{GAB}m_0a_w}{(1 - k_{GAB}a_w)(1 - k_{GAB}a_w + Ck_{GAB}a_w)} \tag{7}$$

where X_{eq} is the equilibrium moisture content, a_w is the water activity, m_0 is the monolayer moisture content and C and k_{GAB} are constants estimated as function of temperature according to following relationships:

$$C = C_0\,\exp\left(\frac{\Delta H_1}{RT}\right) \tag{8}$$

$$k_{GAB} = k_{GAB,0}\,\exp\left(\frac{\Delta H_2}{RT}\right) \tag{9}$$

where T is the absolute temperature, R is the universal gas constant. The values for the whole milk model parameters were taken from the study reported by Lin, Chen and Pearce [33]: $m_0 = 0.04277\ kg/kg$, $\Delta H_1 = 10{,}485\ J/mol$, $C_0 = 0.1925$, $\Delta H_2 = -3215\ J/mol$ and $k_{GAB,\,0} = 2.960$.

The droplet shrinkage was captured by using the linear shrinkage model as a function of the actual moisture content, with the shrinkage factor $b = 0.869$ reported for whole milk at initial solid content of 40% [19]:

$$\frac{d}{d_0} = b + (1 - b)\frac{X}{X_0} \tag{10}$$

2.4. Numerical solution and transient analysis

CFD calculations were undertaken using the pressure-based3D double precision solver in ANSYS FLUENT (Release 2019 R1 & R2). All transport equations were spatially discretized in second order upwind scheme. For spatial discretization of pressure "PRESTO!" scheme was used. The transient formulation followed the second order implicit scheme. The pressure-velocity coupling was undertaken by COUPLED scheme. Turbulence modelling was achieved by using $k - \omega$ SST turbulence model, for which detailed justification can be found elsewhere [34]. For wall boundary conditions, the so-called "enhanced wall treatment" was used, which resolves the viscosity-affected near-wall region all the way to the viscous sublayer for fine meshes and switches automatically from laminar sublayer calculations to the wall function depending on the mesh [35]. The discrete phase (particles) was coupled with the continuous phase using the two-way turbulence coupling and the "reflecting" wall boundary condition with a coefficient of restitution of 1 was employed, which was found reasonable by Jin and Chen [16].

As suggested by Fletcher and Langrish [36], the CFD model was first solved in the steady state framework until a partially converged flow field (still fluctuating flow field) was achieved to provide an initial rough guess for the subsequent transient solution to the model. This usually facilitates the necessary simulation time to develop the transient flow to be significantly reduced, as the steady state already provides a semi-developed flow field. However, interestingly we observed that this method led to inconsistent results. On this note, it is noteworthy that Woo [18] discussed with relation to airflow modelling that for certain spray-drying configurations and operating conditions, the initial steady-state solution could lead to aberrant flow patterns characterized by intense coherent transient flow fluctuations. It was also suggested that using the aberrant flow field as the initial condition for the transient simulation may result in nonphysical results from the transient framework or even divergence of the numerical solution. Therefore, the partially converged flow-field via steady-state solution was discarded and calculation domain was reinitialized using hybrid initialization feature in Fluent and patched with zero velocity throughout to mimic the start-up of the equipment. This served as initial conditions for the transient simulation and thus the entire flow-field was developed in unsteady simulation from scratch. The transient solution was then allowed to progress until a fully developed flow field was achieved. Subsequently the flow time was reset to zero and droplet injection was initiated. The simulation was then allowed to progress until all of the following three criteria were achieved, indicating a fully developed flow with particles: (1) relatively constant number of particles within the chamber, (2) relatively constant outlet temperature, (3) relatively constant outlet humidity. Since in a transient flow field with self-sustained oscillations, achieving a solution characterized by constant parameters such as velocity, temperature, humidity is fairly unusual, the somewhat unspecific characterization "relatively constant" refers to a dynamic solution that fluctuates within the same order of magnitude. All transient analyses reported in the manuscript were undertaken only after this fully developed particle laden flow field was achieved. Numerical implementation of the droplet drying and shrinkage model is not described here for brevity. Interested readers can refer to the following reported previously published by the authors [32].

The selection of the transient time step size was loosely based on the approach reported by Southwell and Langrish [8], in which the time step size was deemed satisfactory if it can capture the transient behavior of the flow field. In addition, we also determined the time step size based on the rule of thumb in which the time step size should be approximately two magnitudes smaller than the characteristic time scale of the system (length of the dryer divide by the inlet velocity). Based on these two factors, the time step size 0.05 s was assumed to be sufficiently refined. In order to corroborate our assumption with some further evidence, only for Case 1 an identical analysis, as presented in this work, with a half time step size i.e. 0.025 s was conducted and it was concluded that the results (not shown here for brevity) were virtually identical.

The mean particle moisture content reported here was averaged from 30 s of transient sampling at the top outlet of the chamber. On top of sampling the particle moisture content, we also sampled the residence time of the particle within the chamber and the time in which the particle was injected into the simulation domain as well as the initial droplet diameter upon injection. With these two pieces of information, we then undertook a pulse-tracer like analysis by filtering and analyzing the residence time distribution of only droplets injected within the initial 1 s of the 30 s sampling time; analogous to an introduction of a 1 s pulse tracer. The frequency distribution of the particle residence time was then analyzed based on their initial droplet diameter.

It is noteworthy that the 30 s of transient particle sampling was about 10 times the theoretical mean residence time (which will be discussed later on). Furthermore, on an average it was found from fast Fourier transform (FFT) of flow fluctuations within the chamber (by monitoring the velocity magnitude at 1.5 m below the inlet at the cylinder-cone interface, roughly at the tip of the high velocity region of the central jet) that the average dominant fluctuation period of the flow field across the runs was found to vary from 1 to 5 s, also approximately 5–10 times smaller than the sampling time scale.

2.5. Calculation of particle motion

The elaboration of the theoretical basics regarding the underlying equations as well as the numerical solution approaches employed in the CFD platform can be found in many standard sources (e.g.

[18,37–39]). For brevity and avoiding repetition we refrain from describing the comprehensive compilation of the theory. However, since the focus of this work is the effect on particle trajectory, for readers' convenience, the relevant details are briefly mentioned in this section. Interested readers can also find further details in the ANSYS® [35] theory guide.

The particle trajectory is calculated by means of integration of the following force balance in the Lagrangian frame of reference:

$$m_p \frac{d\vec{u}_p}{dt} = m_p \frac{18\mu_\infty C_D\, Re}{24\rho_p d_p^2}\left(\vec{u}_\infty - \vec{u}_p\right) + m_p \frac{\vec{g}\left(\rho_p - \rho_\infty\right)}{\rho_p} \tag{11}$$

where m_p, $\vec{u}_p$, d_p and ρ_p are particle (discrete phase) mass, velocity, diameter and density, while $\vec{u}_\infty$, μ_∞ and ρ_∞ represent fluid (continuous phase) velocity, molecular viscosity and density. The term on the left-hand side represent the inertia and the terms on the right-hand side account for the drag force and the force due to gravity respectively. As true particle density 1250 kg/m^3 for whole milk powder is used in this work. However, how the effective density is affected by shrinkage and how this effect is incorporated in the CFD model is elaborately discussed in a previous work [32].

For drag calculations, the drag coefficient C_D for spherical smooth particle is chosen, which is given by the following relationship, where the coefficients a_1, a_2*and* a_3 are given for several ranges of Reynolds number *Re* by Morsi and Alexander [40]:

$$C_D = a_1 + \frac{a_2}{Re} + \frac{a_3}{Re^2} \tag{12}$$

Now, since in the CFD simulations turbulence in the continuous phase is also modelled, in order to account for the effect of turbulence on the particles, in the Eq. (11) in place of the fluid velocity u_∞ the mean velocity $\overline{u}_\infty$ is added to the instantaneous value of the fluctuating gas velocity u'_∞ to predict the turbulent dispersion of particles:

$$u_\infty = \overline{u}_\infty + u'_\infty(t) \tag{13}$$

The turbulent dispersion of particles was predicted using the stochastic tracking (random walk) model. Finally, in this work a two-way coupling approach is employed, which means that in addition to the usual consideration that the particle trajectory is impacted by the continuous phase flow pattern, the opposite effect (the impact of the discrete phase on the continuous phase flow pattern) is included in the calculations as well. This two -way coupling is achieved by alternatingly solving equations pertaining to both phases until the solutions in both phases converge. There are three transfer equations, namely momentum, heat and mass, which account for the transfers of each quantity from the continuous phase to the discrete phase, as the particle passes through each control volume. The equations can be described as follows:

Momentum transfer:

$$F = \sum\left[\frac{18\mu_\infty C_D\, Re}{24\rho_p d_p^2}\left(u_p - u_\infty\right)\right]\dot{m}_p \Delta t \tag{14}$$

Heat transfer:

$$Q = \frac{\dot{m}_{p,0}}{m_{p,0}}\left[\left(m_{p,out} - m_{p,in}\right)\left(\Delta h_{v,i} - \int_{T_{ref}}^{T_{bp}} c_{P,i}dT + \int_{T_{ref}}^{T_{bp}} c_{P,p}dT\right) - m_{p,out}\int_{T_{ref}}^{T_{p,out}} c_{P,p}dT + m_{p,in}\int_{T_{ref}}^{T_{p,in}} c_{P,p}dT\right] \tag{15}$$

Mass transfer:

$$M = \frac{\Delta m_p}{m_{p,0}}\dot{m}_{p,0} \tag{16}$$

The calculated momentum, heat and mass exchange appear as corresponding source terms in the momentum balance, energy balance and continuity equation respectively in any subsequent calculations of the continuous phase flow field.

In the above Eqs. (14)–(16) $\dot{m}_p$, $\dot{m}_{p,0}$, $m_{p,0}$, $m_{p,in}$and $m_{p,\,out}$ represent the mass flow rate of the particles, initial mass flow rate of the particle injection, initial mass of the particle, mass of the particle on cell entry and mass of the particle on cell exit respectively. Furthermore, $c_{P,\,i}$, $c_{P,\,p}$, T_{ref}, $T_{bp,\,i}$, $\Delta h_{v,\,i}$ $T_{p,\,in}$ and,$T_{p,\,out}$ denote the specific heat capacity of the evaporating species and the particle at constant pressure, reference temperature, boiling point and latent heat of evaporation of the evaporating species, temperature of the particle on cell entry and exit respectively.

3. Results and discussion

3.1. Comparison with available experimental data

The prediction from the model followed the experimental trend observed (Table 2). There were, however, discrepancies in the absolute value of the predicted outlet conditions. Overall, the model under predicted the humidity and temperature of the outlet air by an average of 16% and 3% respectively. The relatively higher discrepancy in specific humidity is expected, since at such high temperatures slight error in measurements of relative humidity leads to fairly large difference in specific humidity. As for the powder moisture content, it is important to note that the powder samples of which the moisture contents were measured, were collected from the cyclone outlet (due to being only port available), whereas the simulations predicted the moisture content directly at the chamber outlet. Due to the additional path travelled by the sample and hence having been exposed to disparate air conditions for a longer residence time, it is likely for the powder sample to experience relatively cooler conditions. These cooler conditions would naturally correspond to significantly higher equilibrium moisture contents, which explains the deviations in the prediction. The discrepancies here, nonetheless, fall within the range of error reported in the literature [41] (not many reports give such full validation). It is well-known how challenging it is to closely match the measured data at large scale commercial dryers with predicted results due to a wide variety of uncertainties and non-linearities involved in modelling industrial scale spray dryers. It is noteworthy that in addition to the airflow prediction and the Lagrangian tracking framework, the essential components of the employed CFD model i.e. the sub-models such as the droplet drying model, shrinkage model were already validated using established techniques such as single droplet drying (SDD) [28,42,43] and monodisperse spray drying (MDSD) [44,45] in the past. Therefore, it can be safely assumed that the discrepancies were stemming from the limitations of the measurements due to available access and the whole

Table 2
Comparison of CFD prediction of outlet conditions with measured values.

Quantity	Case 1	Case 2	Case 3	Case 4	Case 6	Case 7	Source
Outlet humidity, g/kg dry air (H3)	22.6	22.4	17.5	23.1	16.4	21.1	Measured
	16.8 ± 0.7	17.9 ± 0.6	17.1 ± 0.6	18.2 ± 0.5	14.6 ± 0.5	20.5 ± 0.8	Simulation
Outlet temp., °C (T3)	111	91	80	75	81	80	Measured
	106 ± 9	88 ± 6	77 ± 5	75 ± 5	77 ± 5	79 ± 6	Simulation
Product moisture content, %wt	1.09	1.65	2.35	2.54	2.82	2.18	Measured
	0.071	0.187	0.321	0.403	0.298	0.331	Simulation

process-based simplifications or assumptions. Nevertheless, despite the discrepancies which fall within the range of previous reports for commercial dryers, as the model prediction followed the experimental trend, it was an indication that model was able to capture the predominant characteristics of the airflow and drying process in the chamber, when the temperature was increased (Run 1 to 4) and when the airflow rate and its velocity was increased (Case 5 through 7).

Please note that even though measurements of Case 5 had been conducted, we later on decided not to perform the simulation work on this, since Case 5 and Case 6 use almost identical operating conditions. Performing simulation would therefore lead to very similar results. We nonetheless decided to keep Case 5 in the Table 1 for firstly completeness of the reporting and secondly for the purpose of demonstrating that in case of a commercial scale dryer the measured bulk properties can be fairly different and hence should not be treated to be as accurate as lab scale experiments, when it comes to the comparison with model predictions.

3.2. Airflow pattern within the chamber

Fig. 5 shows the snap shot of airflow patterns observed within the chamber. In addition to the snapshots provided, Supplementary Videos 1 and 2 are also provided that helps to more clearly discern the airflow patterns discussed here. It was found by carefully analyzing the flow pattern that the central air jet usually tends to hit the conical wall and a small portion of the air bends upwards along the wall. The majority of the air from the deflected jet, however, bends towards the opposite side of the chamber moving upwards. This principal portion of the deflected jet is interestingly also joined by the inlet air from the static fluidized bed. It was mostly observed that these two streams would merge and take the identical side of the chamber. Such merging of the reflected air and the bottom fluidized bed air has been reported before by Gabites, Abrahamson and Winchester [7]. Part of the upwards moving air along the opposite wall may leave the chamber if it reaches the top outlet port, depending on the plane of the deflection. The portion of air which do not leave the top outlet port then traverses the ceiling region of the chamber to mix with the small portion of air which did not bounce upon the jet deflection. Due to the lower pressure caused on the relatively empty side by the merged upward moving streams, the stream traversing along the ceiling is drawn towards that side and start building up or recirculate.

It is noteworthy that the mechanism above is not perfectly symmetrical and the upward moving deflected jet may twist slightly in the circumferential manner. This in effect also creates pressure imbalance

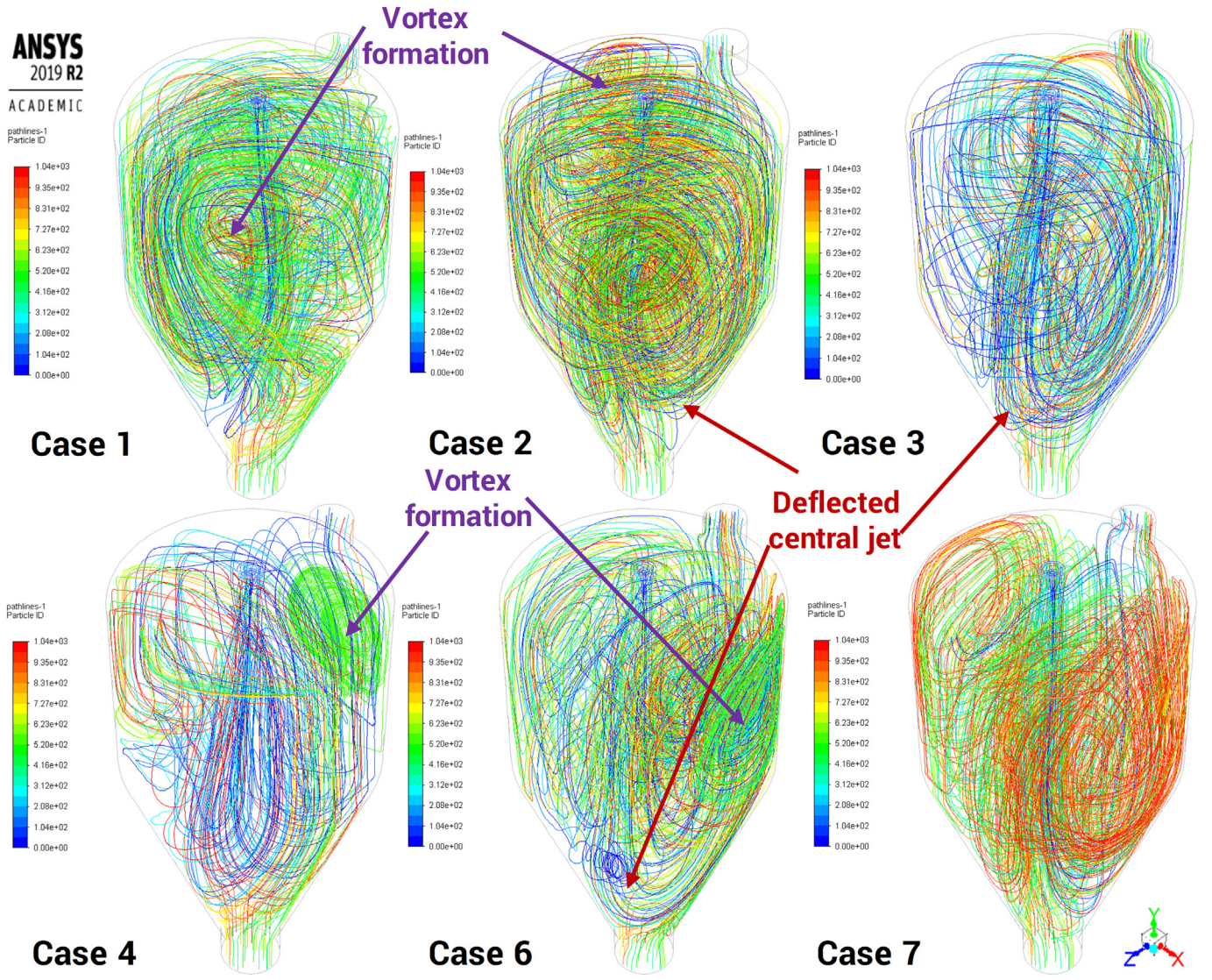

Fig. 5. Comparison of the instantaneous flow field from the simulations for all tested cases at a flow time of 60 s. Pathlines are colored by the particle ID. (For more insight into the predicted flowfields, please view the solution videos available online; Comparison by means of long pathlines (Video 1) as well as short pathlines (Video 2) among all cases).

along the circumference of the chamber which essentially rotates the deflecting jet. Therefore, in analysis of the shorter pathlines of the airflow within the chamber (Supplementary Video 2), it can be seen that the deflected part of the jet also experiences rotation which creates a self-sustained upwards sweeping region along the chamber wall.

The airflow pattern above effectively creates transient vortices between the regions of the high and low velocities (shown with violet arrows in Fig. 5), particularly at regions away from the upwards deflected jet. Following the rotating nature of the deflecting jet, the transient vortices also move around the chamber in a chaotic manner with no fixed pattern (Fig. 5). An interesting observation was that once the rotating vortices reach the top outlet port, they breakdown, most probably due to the disruption caused by the air leaving the chamber. From the video, it was difficult to quantitatively distinguish the fluctuation frequency of the central jet rotation or the frequency of the transient formation of the vortices among various cases. This can be nonetheless indirectly discussed in a qualitative manner by analyzing the fluctuation frequency of the central jet under these different cases.

Taking Case 6, 1, 2, 3, 4 and 7 (descending order of inlet hot air velocity) for comparison, the vortices in Case 6 qualitatively appear to be the most frequently formed and the vortices were more distinct while oscillating along the circumference of the chamber wall before they broke down as they approached the top outlet region. From the supplementary video, it can be clearly discerned that the frequency and the distinction of the vortices pair is reduced with reducing chamber velocity. This may be due to the more rapid self-sustained rotation of the deflected central jet at higher airflow velocity within the chamber. It must be noted that the discussed contrast is clearly noticeable between the two extreme cases 6 and 7, while the differences among the rest of the cases in between may not be that clearly visible. The supplementary video with the shorter pathline (Video 2) clearly illustrates the difference in rotation behavior.

Before we present the Fast Fourier Transform (FFT) analysis on the fluctuations, the comparison of the velocity components monitored at 2 points situated on the *Z*-axis and 1.5 m below the inlet are shown in Fig. 6 (Case 1, 2 and 3) and Fig. 7 (Case 4, 6 and 7). By comparing the axial components (the graphs in the middle, particularly the green colored lines), we can see that the variation of the primary hot inlet air velocity is accordingly translated into the difference in the average velocity magnitudes (Cases sorted according to the axial velocity magnitudes ranked in an ascending order leads to Case 7 < Case 4 < Case 1 < Case 6), as expected. It was however interesting to see that the case 2 and 3 occasionally reached slightly higher magnitudes than case 1, even though the primary hot air inlet velocity was much higher for case 1. On the other hand, the fluctuations were more frequent in case 1. It is noteworthy that the significant difference among case 1, 2, 3 and 4 is the inlet temperature (250 °C, 215 °C, 191 °C and 186 °C respectively), while the mass flow rates are similar. This indicates that the higher energy content of the stream (ultimately leading to a higher inlet velocity and a lower density in the calculation model) is likely to be translated into fluctuations with more noise like elements, whereas the decrease in temperature leads to relatively smoother fluctuations.

Comparison of the radial (x and z) components led to the finding that the magnitudes of the x-components were higher, whereas the fluctuations in z-components were found to occur more frequently. Furthermore, the alternating positive and negative values of the radial components showed that the jet was rotating fairly randomly (no pattern was evident) and yet across the entire plane, i.e. the jet showed no bias towards any corner or side (better visible in the supplementary Videos 1 and 2).

FFT is a widely used technique in analyzing the flow characteristics of transient air flow pattern with self-sustained oscillations [5,36]. Fig. 8 shows the FFT of the velocity components of the central jet corresponding to the cartesian coordinates shown in Fig. 3. The fluctuation of the axial component did not reveal any significant differences between the cases, except for the case 7, which showed markedly fewer characteristic peaks (0 Hz point is a numerical discrepancy and should not be interpreted). The dominant frequencies for those peaks were clearly identifiable between 0.1 and 0.2 Hz. This indicates that the

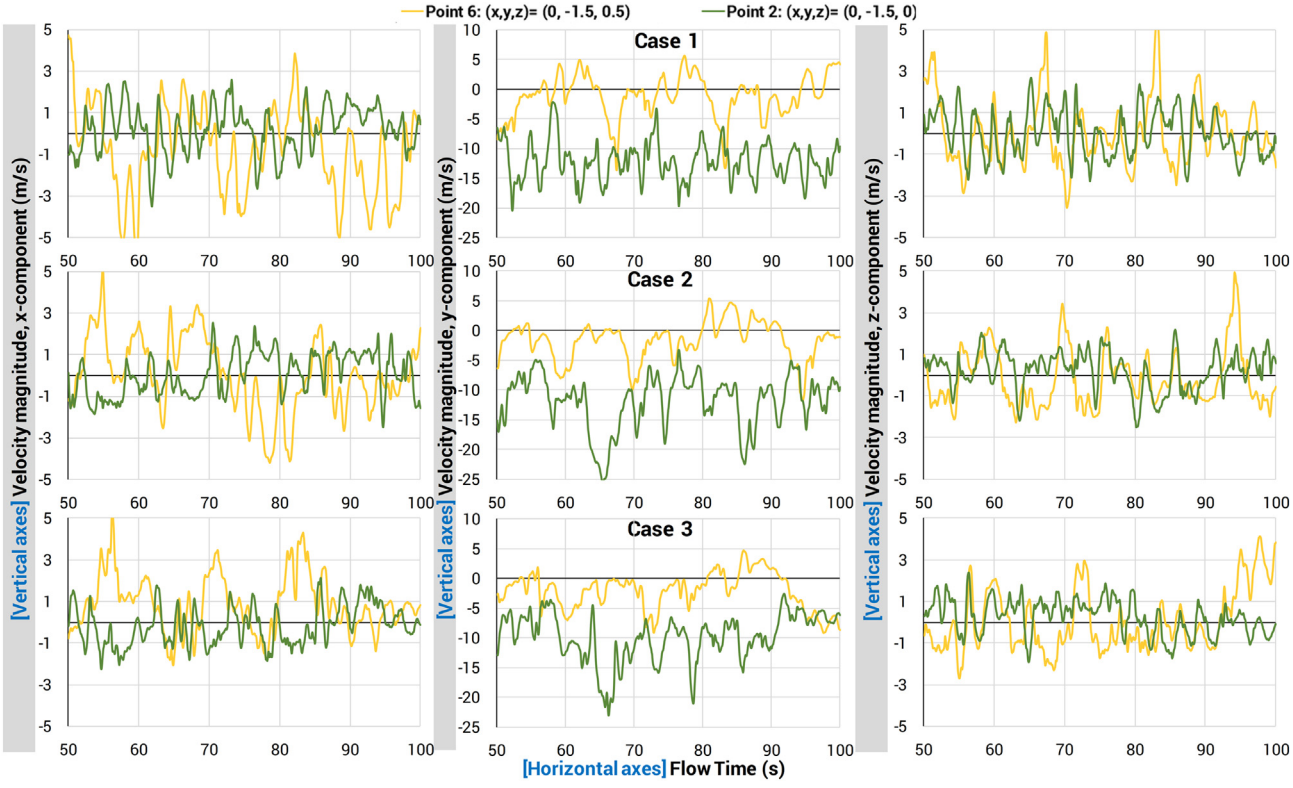

Fig. 6. Comparison of velocity (magnitude of x, y and z component of the velocity) profiles among case 1 through 3 monitored at the points 6 (0, −1.5, 0.5), 2 (0, −1.5, 0) and 8 (0, −1.5, −0.5).

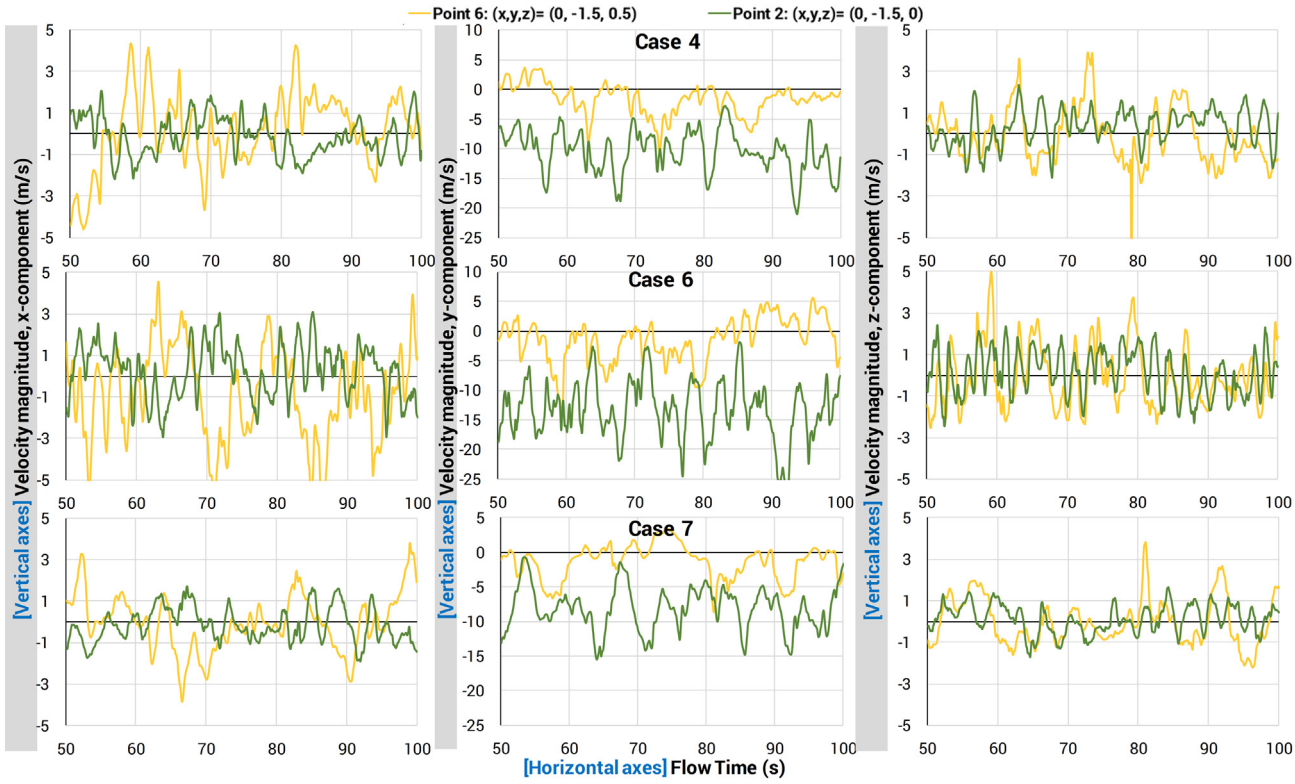

Fig. 7. Comparison of velocity (magnitude of x, y and z component of the velocity) profiles among cases 4, 6 and 7 monitored at the points 6 (0, −1.5, 0.5), 2 (0, −1.5, 0) and 8 (0, −1.5, −0.5).

axial flow in case 7 was less irregular, when compared to other cases, particularly case 6, which was the most representative of a more chaotic flow. This observation suggests that the higher mass flow rates and hence higher velocities are more likely to cause chaotic fluctuations. Analysis on the radial components revealed higher inlet velocity led to high frequency characteristic peaks. Surprisingly, the characteristic peaks for each case is different in the x and z velocity component. While both directions seem to have characteristic peaks in the frequency region (0.2–0.5 Hz), the x-component seemed to exhibit a more coherent characteristics, as the peaks were found at similar frequency (around 0.4 Hz), whereas those for z-components were comparatively more scattered. It is noteworthy that fluctuation in the z direction indicates fluctuation in the plane of the top outlet ports while the x direction is perpendicular to the outlet plane. From Fig. 8 it is evident that quantitatively more peaks for z-components were found than those for the x-components. This indicates that the position of the outlet affects the oscillation making the airflow oscillate more in the plane of the outlets, perhaps because of the proximity to the vacuum exerted on the outlet had led to the more pronounced fluctuations observed.

3.3. Particle movement within the chamber

The fluctuating and rotating flow field led to two distinct patterns of transient particle clustering within the chamber. The first distinct structure is the clustering of particles originating at the top of the conical region (just below the cylindrical-conical wall interface) (Fig. 9). Surprisingly, the particle cluster temporarily exhibited moments of close to zero velocity, as if it were suspended within the chamber before progressively traveling upwards corresponding to the rotating upwards sweep of the deflected central jet described earlier and finally dispersed. This observation indicates that the particle clustering initially occurred at regions of low velocity caused by the jet deflection as shown in Fig. 5. Similar upwards movement of particle clouds mostly made up of medium sized particles (224–285 μm) was reported in a previous study [16]. The particle cloud in their study reportedly stayed close to conical wall and in contrast to the traveling of the particle cluster in this study around the chamber (conical, cylindrical and ceiling regions), would disperse as soon as it reached the cylindrical section of the dryer. Nevertheless, similar to our findings, the particle cluster coincided with the vortices of the air phase.

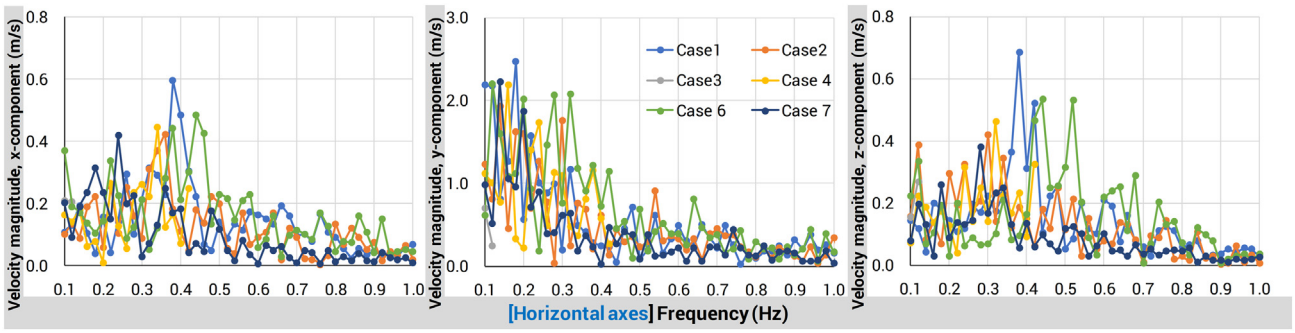

Fig. 8. Fast Fourier Transform of the component velocity magnitudes i.e. x component (left), axial velocity/y component (middle) and z-component (right) monitored at Point 2 (0, −1.5, 0).

The other coherent structure observed from the simulation is the formation of clusters corresponding to the transient vortex formation in the flow field. Similar to the observation in air flow field analysis, these two coherent particle cluster structures near the wall regions of the chamber was less distinct and less frequent for cases with lower inlet hot air mass flow rate (lower velocity). This is clearly noticeable in the supplementary videos (See Videos 3 and 4 for comparison of tracked particles colored by residence time and water mass fraction respectively among all cases). An interesting observation here must be noted that due to the transient nature of the vortex, the clustered particles may not necessarily be those particles having the longest residence times within the chamber. Qualitatively, these clustered particles within the vortex exhibited residence times in the intermediate range of the total residence time within the chamber (see Fig. 9 for the dominant light blue color occurring in the clusters).

Having discussed the observations of these coherent transient particle clusters, it is important to further discuss the particle movement pattern within the chamber which leads to the particle leaving the chamber via the top outlet. From the video observations, it appeared that the particles were continuously leaving the top outlet. These are mainly those particles which are not trapped in the coherent clusters discussed above. In addition to those free particles, there are, nonetheless, sudden 'gushes' or transports of particle to the top section of the chamber (bringing the particle closer or towards the outlet) due to the transient upwards deflected central jet recirculation and its upwards sweep discussed earlier. While such upwards sweeps carry sudden gushes of clustered particles towards the top outlet, it can be expected that the upwards sweep may also entrain some 'freshly injected' particles form the nozzle towards the top outlet. These fresh particles, due to the high velocity of the central jet, have relatively lower chamber residence time. There are also sudden gushes of particles leaving the top outlet when the vortices rotate circumferentially and reaches the outlet. Therefore, the formation of vortices under different operating conditions is likely to directly influence the particle residence time distribution (which will be discussed next) within the chamber.

3.4. Particle tracer residence time analysis

As a theoretical benchmark for comparison, if one were to assume that there is no transient flow fluctuation in the chamber, the central

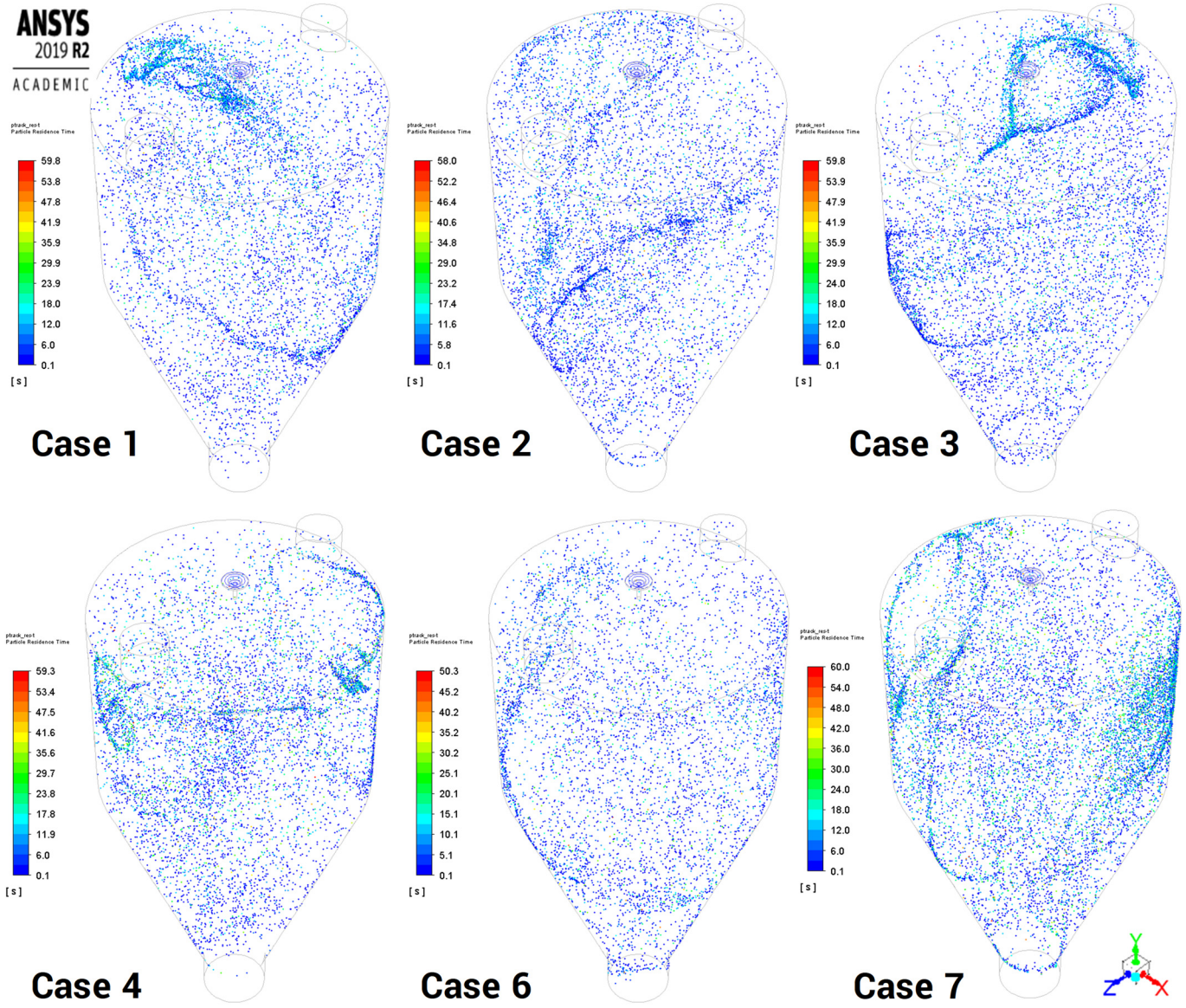

Fig. 9. Comparison of the snap shots of tracked particles from the simulations for all tested cases at a flow time of 60 s. Particles are colored by the residence time. (For more insight into the particle movements inside the chamber, please view the solution videos available online; Videos 3 and 4 for tracked particles colored by residence time and water mass fraction respectively).

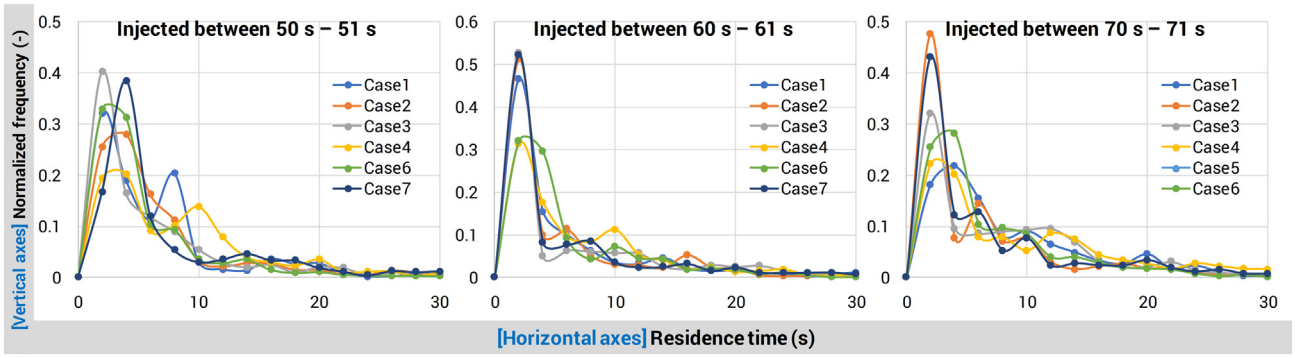

Fig. 10. Comparison of the predicted residence time distributions of the particles injected between flow times 50 s and 51 s (left), 60 s and 61 s (middle), 70 s and 71 s (right) among all tested cases.

jet should simply enter the chamber and when it reaches the conical wall, should uniformly (circumferentially) recirculate back upwards towards the top outlet. The recirculated upwards flow would thereby be supplemented by the inlet air flow via the bottom fluidized bed. In an ideal condition, if the particles follow the air-flow pattern, they would travel approximately double the height of the cylindrical and conical region of the tower. Based on these assumptions, an ideal theoretical particle residence time benchmark was approximated (calculation method given in the supplementary information). According to the employed method a rough ideal theoretical particle residence time can be approximated by dividing twice the length of the tower with the respective characteristic air flow velocities at each section of the chamber.

The theoretical benchmark particle residence time calculated for the cases in this work lies within the range of 7.5–10.1 s. In contrast, the particle residence time distribution of the tracer particles, tracer numerically injected three times into the simulation (Fig. 10), showed mode particle residence time of about 2–5 s, approximately half of the theoretical benchmark (amendment to estimation of the theoretical benchmark follows in the later part of the discussion). It is noteworthy that the slight differences in the residence time distributions among the different time of initiation of the tracer analysis again clearly reflects the transient nature of the air flow patterns and the impact thereof on the particle residence time. Therefore, to be able to comment on a more representative residence time distribution in Fig. 11a the three tracer analyses discussed above along with three further tracer analyses (80–81 s, 90–91 s and 100–101 s) were merged to calculate and show a single representative distribution for each case. Yet the observation regarding the underprediction of residence time with respect to the theoretical benchmark was consistent across all the different cases evaluated. The shorter particle residence time relative to the ideal theoretical benchmark can only occur due to higher localized airflow velocity within the chamber caused by the deflection of the central jet. If we reduce the cross-section area in the theoretical benchmark calculation and thus the volume available for the upwards recirculation of the air flow of the jet to a quarter (to arbitrarily mimic the non-ideality), the theoretical particle residence time would be between 2.2 and 2.9 s, which falls within the similar range of the numerically determined mode particle residence time via simulations. Therefore, this can be considered evidence for the fact that the upwards particle sweeping by the central jet effectively reduces the particle residence time for a certain portion of the particles. While this phenomenon reduces the overall residence time of the particles, it does not mean that the recirculated airflow due to the central jet fluctuation always reduces the residence time of all the particles. Particle which were not removed with the upwards gush may still be trapped in the recirculated airflow and this is manifested in the skewed distribution with multiple minor secondary peaks and a trailing off edge at the longer residence time. Even at the end of the 30 s tracer tracking, some of the tracer particles were still being detected indicating that the residence time of the particles in the chamber may as well exceed 30 s, albeit for a very small percentage of the particles.

Further analysis revealed that there is no definite correlation of these longer residence time particles with the particles size. On this note, it should be noted that Zbicinski, Strumillo and Delag [46] in their comprehensive experimental study also made similar observations and the particle residence time was reported to be usually shorter than

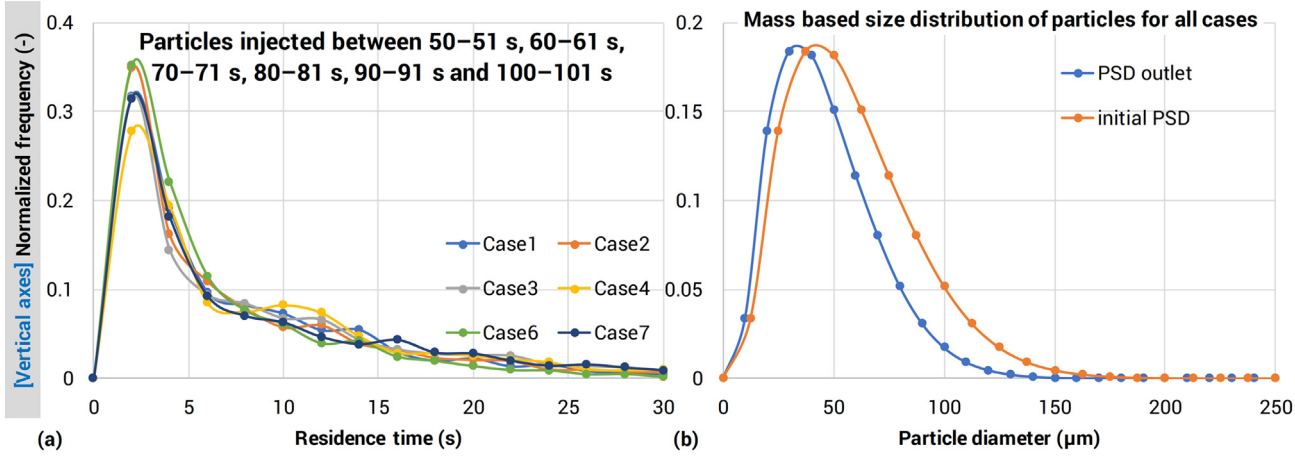

Fig. 11. Comparison of the (a) predicted residence time distributions of all particles injected between flow times 50 s and 51 s, 60 s and 61 s, 70 s and 71 s, 80 s and 81 s, 90 s and 91 s, 100 s and 101 s combined together among all tested runs; (b) The particle size distribution (PSD) at the outlet that were found to be similar for all cases, with the initial PSD.

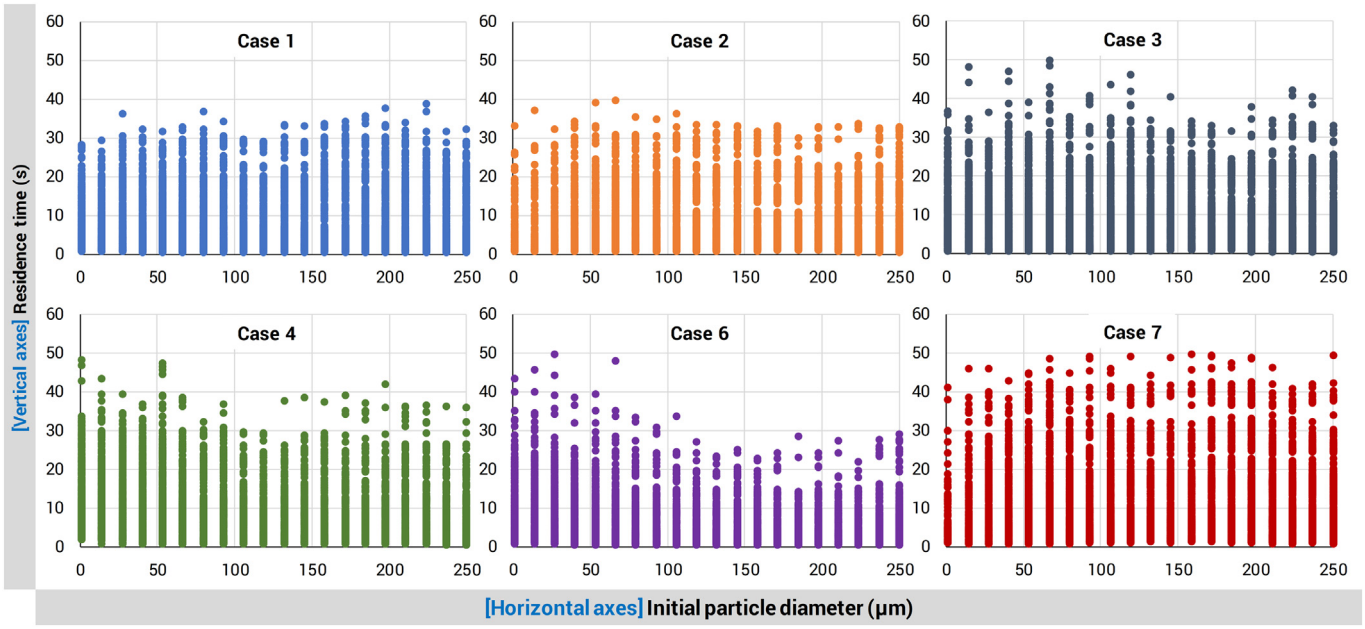

Fig. 12. Scatter plot to exhibit the predicted correlation between tracer particle residence time and particle size distribution.

that of the drying medium i.e. air. As Fig. 12 clearly depicts for all cases, the predicted residence times are fairly uniformly distributed across the range of particle diameters. Obviously, there is a slight bias for the fine fraction to have a slightly longer residence time. The finer the particles are, the more likely they are to closely follow the airflow pattern and get trapped in these self-sustained recirculating flow structure. This effect is evidently pronounced for the highest inlet velocity, which is case 6. Moreover, the most uniformly distributed residence time is observed for the case 7, which had the slowest air movement inside the chamber. This is evidence for the intriguing conclusion that particle entrapment in air recirculation is only significant when the flow velocity is high. It is noteworthy that no matter how small the air velocity was inside the chamber, for all cases the upward velocity was greater than the terminal velocity (approximately in the range of 0.3–1.7 m/s) estimated for all the particles (for particle size distribution see Fig. 11b). As a result, no significant fraction was collected at the static fluidized bed. This was also accordingly reflected in the simulations.

Another particularly interesting trend observed from the numerical particle residence time tracing is the 'bump' in the distribution between 5 and 12 s period of the distribution. Depending on the moment of tracer injection (due to the random fluctuating behavior of the flow field), these bumps may be quite significant leading to bimodal peaks in the residence time distribution. This suggests that the particles detected within this range of residence time may have been influenced by a coherent flow mechanism and hence are not just randomly transported particles leaving the chamber. In view of the fact that this range also corresponds to the intermediate range of residence time predicted and is higher than that of the coherently upward swept particles, we speculate that such spikes may have been caused by the clustered particles in vortices reaching and leaving the top outlet ports.

From the stochastic and random nature in the variation of the numerical tracer analysis results (see Figs. 10–12), we could not find any significant differences between the cases evaluated, in terms of the particle residence time distribution. This was an unexpected finding, particularly considering the contrasting inlet air velocity used and the significantly different airflow fluctuation observed, especially between Case 6 and Case 7. This further suggests that the coherent upwards sweeping of the particle by the deflected and recirculated jet is more significant in determining the bulk of the particle residence time rather than the fluctuation patterns normally discussed in the literature [4–6,10,47,48]. What does this mean for spray drying design? Future design of spray dryers should take the self-sustained fluctuation phenomenon into consideration. The deflection of the central jet will have the tendency to decrease the overall particle residence time within the chamber. This, in addition to the generation of recirculation flow, is leading to a wide range of long residence time particles. In this report, we have introduced a simplified approach to estimate the particle residence time within the type of drying chamber evaluated, which in combination with the simulation prediction can lead to a more accurate design of the spray dryers.

4. Conclusions

In this study the spray drying of whole milk was simulated with the commercial CFD package ANSYS FLUENT. The CFD model included drying kinetics and turbulent dispersion of the particles, while ignoring the particle collision and the subsequent phenomena such as wall-deposition, coalescence and agglomeration. Nevertheless, the simulation results could be corroborated with experimental data from 6 different trials in terms of bulk property measurements such as outlet air temperature, humidity and powder moisture content. Then the CFD simulations were analyzed in detail to investigate the air flow patterns and their effect on the particle movement and residence time.

Numerical analysis on the commercial scale cylinder-on-cone spray dryer with a bottom static fluidized bed revealed two coherent transient flow structures: (1) rotating upwards flow along the chamber wall caused by the rotating central jet deflection and (2) transient vortices in regions away from the upwards flowing deflected jet. Higher inlet velocity led to more significant fluctuating behavior, while lower inlet temperatures led to relatively smoother fluctuations. The air flow patterns led to formation of particle clusters in the regions closer to the wall corresponding to the transient vortices in the air phase. These were found to be fairly dynamic in terms of the participating particles and travelled around the chamber before leaving it following the collapse of the vortices. While air recirculation due to the transient flow structure led to relatively long particle chamber residence time, the rotating and upwards moving flow structure, unexpectedly, reduced the overall mean particle chamber residence time. The transient vortices also led to 'sporadic' burst of particles in the intermediate chamber residence time range. A simplified approach was introduced in this work to

estimate a theoretical mean residence time benchmark for the particles, which can be implemented as a useful tool in designing and scaling up of spray dryers. In conclusion, this work showed that transient flow behavior in the commercial type of spray drying configuration evaluated in this work actually reduces the overall particle residence time in the chamber, albeit generating a wider distribution in the range of chamber residence time. This is an important airflow phenomenon which needs to be taken into consideration in the design of spray dryers and in the estimation of the residence time in a spray dryer.

Supplementary data to this article can be found online at https://doi.org/10.1016/j.powtec.2019.11.023.

Notation

Latin letter

a_1, a_2, a_3	empirical constants in correlation of drag coefficient
a_w	water activity (−)
A	surface area (m^2)
b	shrinkage factor (−)
c_p	specific heat capacity at constant pressure ($Jkg^{-1}\ K^{-1}$)
C	constants in GAB model (−)
C_D	drag coefficient (−)
d	diameter (−)
D	diffusivity ($m^2\ s^{-1}$)f drying rate retardation factor in CDC model (−)
F	force (N)
g	acceleration due to gravity (ms^{-2})
h	heat transfer coefficient ($Wm^{-2}\ K^{-1}$)
h_m	mass transfer coefficient (ms^{-1})
Δh_v	latent heat of vaporization (Jkg^{-1})
ΔH	heat of water sorption ($J\ mol^{-1}$)
k	thermal conductivity ($Wm^{-1}\ K^{-1}$)
k_{GAB}	proportionality constant in GAB model (−)
m	mass (kg)
m_0	monolayer moisture content (−)
Nu	Nusselt number (−)
Pr	Prandtl number (−)
Re	Reynolds number (−)
Sh	Sherwood number (−)
Sc	Schmidt number (−)
t	time (s)
T	temperature (K)
u	velocity (ms^{-1})
V	volume (m^3)
$\dot{V}$	volumetric flow rate ($m^3\ s^{-1}$)
x	normalized moisture content (−)
X	dry basis moisture content (kg H_2O/kg solid)

Greek letter

Δ	difference (−)
μ	dynamic viscosity ($kg\ m^{-1}\ s^{-1}$)
ρ	density ($kg\ m^{-3}$)

Subscripts

0	initial
∞	environment/bulk
a	air
bp	boiling point
cr	critical
eq	equilibrium
i	component index/initial/inlet
m	mass
o	outlet
p	particle
$surf$	surface
ref	reference

Declaration of Competing Interest

The authors declare that they have no known competing financial interests or personal relationships that could have appeared to influence the work reported in this paper.

Acknowledgements

The first author acknowledges the support provided by the Australian Government Department of Industry, Innovation, and Science through the Australia-China Science and Research Fund (ACSRF48154), as part of the research program of the Australia-China Joint Research Centre in Future Dairy Manufacturing (http://acjrc.eng.monash.edu/). Soochow University acknowledges The National Key Research and Development Program of China (International S&T Cooperation Program, ISTCP, 2016YFE0101200) for support of the Australia-China collaboration. Furthermore, the corresponding author acknowledges the Outside Study Programme of the Faculty of Engineering, Monash University supporting crucial experimental components of this work undertaken in France.

References

[1] J. Pisecký, Handbook of Milk Powder Manufacture, GEA Process Engineering A/S (GEA Niro), Copenhagen, Denmark, 1997.
[2] V. Westergaard, Milk Powder Technology: Evaporation and Spray Drying, GEA Niro A/S, Copenhagen, 2004.
[3] K. Masters, Spray Drying Handbook, 5th ed. Longman Scientific and Technical, New York, 1991.
[4] T.A.G. Langrish, J. Williams, D.F. Fletcher, Simulation of the effects of inlet swirl on gas flow patterns in a pilot-scale spray dryer, Chem. Eng. Res. Des. 82 (2004) 821–833.
[5] M.W. Woo, W.R.W. Daud, A.S. Mujumdar, Z. Wu, M.Z.M. Talib, S.M. Tasirin, Non-swirling steady and transient flow simulations in short-form spray dryers, Chem. Prod. Process. Model. 4 (2009)Article 20.
[6] B. Guo, T.A.G. Langrish, D.F. Fletcher, Simulation of gas flow instability in a spray dryer, Chem. Eng. Res. Des. 81 (2003) 631–638.
[7] J.R. Gabites, J. Abrahamson, J.A. Winchester, Air flow patterns in an industrial milk powder spray dryer, Chem. Eng. Res. Des. 88 (2010) 899–910.
[8] D.B. Southwell, T.A.G. Langrish, Observations of flow patterns in a spray dryer, Dry. Technol. 18 (2000) 661–685.
[9] F.G. Kieviet, J. Van Raaij, P.P.E.A. De Moor, P.J.A.M. Kerkhof, Measurement and modelling of the air flow pattern in a pilot-plant spray dryer, Chem. Eng. Res. Des. 75 (1997) 321–328.
[10] B. Guo, T.A.G. Langrish, D.F. Fletcher, Numerical simulation of unsteady turbulent flow in axisymmetric sudden expansions, J. Fluids Eng. 123 (2001) 574–587.
[11] A. Mataoui, R. Schiestel, Unsteady phenomena of an oscillating turbulent jet flow inside a cavity: effect of aspect ratio, J. Fluids Struct. 25 (2009) 60–79.
[12] B. Guo, T.A.G. Langrish, D.F. Fletcher, Simulation of turbulent swirl flow in an axisymmetric sudden expansion, AIAA J. 39 (2001) 96–102.
[13] D.F. Fletcher, B. Guo, D.J.E. Harvie, T.A.G. Langrish, J.J. Nijdam, J. Williams, What is important in the simulation of spray dryer performance and how do current CFD models perform? Appl. Math. Model. 30 (2006) 1281–1292.
[14] K. Kota, T. Langrish, Prediction of deposition patterns in a pilot-scale spray dryer using computational fluid dynamics (CFD) simulations, Chem. Prod. Process. Model. 2 (2007) 1–18.
[15] D.E. Oakley, Spray dryer modeling in theory and practice, Dry. Technol. 22 (2004) 1371–1402.
[16] Y. Jin, X.D. Chen, Numerical study of the drying process of different sized particles in an industrial-scale spray dryer, Dry. Technol. 27 (2009) 371–381.
[17] R. Jeantet, F. Ducept, A. Dolivet, S. Méjean, P. Schuck, Residence time distribution: a tool to improve spray-drying control, Dairy Sci. Technol. 88 (2008) 31–43.
[18] M.W. Woo, Computational Fluid Dynamics Simulation of Spray Dryers: An Engineer's Guide, CRC Press, Boca Raton London New York, 2016.
[19] S.X.Q. Lin, X.D. Chen, Engineering data of diameter change during air drying of milk droplets with 40 wt% initial solids content, Dry. Technol. 27 (2009) 1028–1032.
[20] L. Huang, Simulation of Spray Dryers Using Computational Fluid Dynamics, National University of Singapore, 2005.
[21] R.B. Keey, M. Suzuki, On the characteristic drying curve, Int. J. Heat Mass Transf. 17 (1974) 1455–1464.
[22] T.A.G. Langrish, T.K. Kockel, The assessment of a characteristic drying curve for milk powder for use in computational fluid dynamics modelling, Chem. Eng. J. 84 (2001) 69–74.
[23] X.D. Chen, The basics of a reaction engineering approach to modeling air-drying of small droplets or thin-layer materials, Dry. Technol. 26 (2008) 627–639.
[24] X.D. Chen, S.X.Q. Lin, Air drying of milk droplet under constant and time-dependent conditions, AICHE J. 51 (2005) 1790–1799.
[25] M.W. Woo, W.R.W. Daud, A.S. Mujumdar, M.Z.M. Talib, W.Z.T. Hua, Siti Masrinda, Comparative study of droplet drying models for CFD modelling, Chem. Eng. Res. Des. 86 (2008) 1038–1048.

[26] M.W. Woo, W.R.W. Daud, A.S. Mujumdar, Z. Wu, M.Z. Meor Talib, S.M. Tasirin, CFD evaluation of droplet drying models in a spray dryer fitted with a rotary atomizer, Dry. Technol. 26 (2008) 1180–1198.
[27] J.H. Chew, N. Fu, M.W. Woo, K. Patel, C. Selomulya, X.D. Chen, Capturing the effect of initial concentrations on the drying kinetics of high solids milk using reaction engineering approach, Dairy Sci. Technol. 93 (2013) 415–430.
[28] S.X.Q. Lin, X.D. Chen, Changes in milk droplet diameter during drying under constant drying conditions investigated using the glass-filament method, Food Bioprod. Process. 82 (2004) 213–218.
[29] S.X.Q. Lin, Drying of Single Milk Droplet, PhD Dissertation Department of Chemical Engineering, The University of Auckland, 2004.
[30] W.E. Ranz, W.R. Marshall, Evaporation from drops part 1, Chem. Eng. Prog. 48 (1952) 141–146.
[31] W.E. Ranz, W.R. Marshall, Evaporation from drops part 2, Chem. Eng. Prog. 48 (1952) 173–180.
[32] H. Jubaer, S. Afshar, J. Xiao, X.D. Chen, C. Selomulya, M.W. Woo, On the importance of droplet shrinkage in CFD-modeling of spray drying, Dry. Technol. 36 (2018) 1785–1801.
[33] S.X.Q. Lin, X.D. Chen, D.L. Pearce, Desorption isotherm of milk powders at elevated temperatures and over a wide range of relative humidity, J. Food Eng. 68 (2005) 257–264.
[34] H. Jubaer, S. Afshar, J. Xiao, X.D. Chen, C. Selomulya, M.W. Woo, On the effect of turbulence models on CFD simulations of a counter-current spray drying process, Chem. Eng. Res. Des. 141 (2019) 592–607.
[35] ANSYS® FLUENT, Help System, ANSYS FLUENT Theory Guide, Release 2019R2, ANSYS, Inc, USA, 2019.
[36] D.F. Fletcher, T.A.G. Langrish, Scale-adaptive simulation (SAS) modelling of a pilot-scale spray dryer, Chem. Eng. Res. Des. 87 (2009) 1371–1378.
[37] S. Patankar, Numerical Heat Transfer and Fluid Flow, CRC press, 1980.
[38] H.K. Versteeg, W. Malalasekera, An Introduction to Computational Fluid Dynamics: The Finite Volume Method, Pearson Education, 2007.
[39] E. Loth, Computational methods: overview of numerical approaches, in: E.E. Michaelides, C.T. Crowe, J.D. Schwarzkopf (Eds.), Multiphase Flow Handbook, CRC Press, Boca Raton London New York 2016, pp. 79–95.
[40] S.A. Morsi, A.J. Alexander, An investigation of particle trajectories in two-phase flow systems, J. Fluid Mech. 55 (1972) 193–208.
[41] K. Patel, X.D. Chen, R. Jeantet, P. Schuck, One-dimensional simulation of co-current, dairy spray drying systems — pros and cons, Dairy Sci. Technol. 90 (2010) 181–210.
[42] S.X. Qi Lin, X.D. Chen, Improving the glass-filament method for accurate measurement of drying kinetics of liquid droplets, Chem. Eng. Res. Des. 80 (2002) 401–410.
[43] L. Che, X.D. Chen, A simple nongravimetric technique for measurement of convective drying kinetics of single droplets, Dry. Technol. 28 (2009) 73–77.
[44] S. Rogers, W.D. Wu, S.X.Q. Lin, X.D. Chen, Particle shrinkage and morphology of milk powder made with a monodisperse spray dryer, Biochem. Eng. J. 62 (2012) 92–100.
[45] X. Yang, J. Xiao, M.-W. Woo, X.D. Chen, Three-dimensional numerical investigation of a mono-disperse droplet spray dryer: validation aspects and multi-physics exploration, Dry. Technol. 33 (2015) 742–756.
[46] I. Zbicinski, C. Strumillo, A. Delag, Drying kinetics and particle residence time in spray drying, Dry. Technol. 20 (2002) 1751–1768.
[47] D.J.E. Harvie, T.A.G. Langrish, D.F. Fletcher, Numerical simulations of gas flow patterns within a tall-form spray dryer, Chem. Eng. Res. Des. 79 (2001) 235–248.
[48] D.B. Southwell, T.A.G. Langrish, D.F. Fletcher, Process intensification in spray dryers by turbulence enhancement, Chem. Eng. Res. Des. 77 (1999) 189–205.